Research Article | Vol. 28, No. 10 / 11 May 2020 / Optics Express 14536

Optics EXPRESS

Imaging of surface plasmon polaritons in low-loss highly metallic titanium nitride thin films in visible and infrared regimes

MENA N. GADALLA,* KUNDAN CHAUDHARY, CHRISTINE M. ZGRABIK, FEDERICO CAPASSO, AND EVELYN L. HU

John A. Paulson School of Engineering and Applied Sciences, Harvard University, Cambridge, Massachusetts 02138, USA
mgadalla@g.harvard.edu

Abstract: Titanium nitride (TiN) has been identified as a promising refractory material for high temperature plasmonic applications such as surface plasmon polaritons (SPPs) waveguides, lasers and light sources, and near field optics. Such SPPs are sensitive not only to the highly metallic nature of the TiN, but also to its low loss. We have formed highly metallic, low-loss TiN thin films on MgO substrates to create SPPs with resonances between 775-825 nm. Scanning near-field optical microscopy (SNOM) allowed imaging of the SPP fringes, the accurate determination of the effective wavelength of the SPP modes, and propagation lengths greater than 10 microns. Further, we show the engineering of the band structure of the plasmonic modes in TiN in the mid-IR regime and experimentally demonstrate, for the first time, the ability of TiN to support Spoof Surface Plasmon Polaritons in the mid-IR (6 microns wavelength).

1. Introduction

Recently, there has been growing interest in the exploration of *refractory plasmonic materials*, which can demonstrate superior behavior at elevated temperatures and powers, compared to the more commonly used gold and silver [1,2]. TiN has demonstrated its capabilities as such a refractory material, and several studies have demonstrated thin films of highly metallic TiN, with large negative values of the real part of the material permittivity [Re (ε)] using different deposition techniques such as magnetron sputtering [1,3–7], nitrogen-plasma-assisted molecular-beam epitaxy [8], and pulsed laser deposition [9]. In this paper we optimize the formation of TiN thin films on MgO to achieve both large negative values of Re (ε), as well as small values of Im (ε). Such TiN films are ideally suited to demonstrate *surface plasmon polariton (SPP) resonances* with long propagation lengths. Surface Plasmon Polaritons (SPPs) are coupled states between photons and plasma oscillations that are localized along the interface between a plasmonic material and a dielectric. Currently, SPPs with long surface propagation distances are being considered as the basis of interconnects [10,11], enabling photonic information processing. The robustness of SPP resonances and propagation lengths is sensitive to both the highly metallic nature of the plasmonic material and to its low loss. The high quality of our TiN thin films is demonstrated in the SPP resonances supported in the 775-825 nm wavelength range. Moreover, we are able to directly image the SPP fringes using SNOM. This near-field assessment allows us to determine the effective wavelengths of the SPP modes, and to measure propagation lengths greater than 10 microns. We are able to extend SPPs to much longer wavelengths (6 microns) through the creation of *Spoof SPPs* by patterning the TiN to alter its dispersion characteristics. To guide and calibrate our studies, we carried out a full simulation of the Air/TiN/MgO structures used to model and understand the dispersion relations of the plasmon modes. In aggregate, we believe that the highly metallic and low loss properties of our TiN plasmonic films extend the range of SPP-enabled sensing and communications to higher temperatures made possible by refractory TiN.

#391482 https://doi.org/10.1364/OE.391482
Received 27 Feb 2020; revised 1 Apr 2020; accepted 2 Apr 2020; published 28 Apr 2020

Optics EXPRESS

2. Low loss TiN thin film deposition and dispersion analysis

Highly metallic TiN thin films were reactively sputtered onto <100> MgO substrates at a substrate temperature of 700 °C, 200 V applied substrate bias, and with the ratio of argon to nitrogen equal to 12:4 sccm. The deposition pressure was held at 4 mT with base pressure of the sputtering chamber of around 5×10^{-8} Torr. These conditions were optimized to improve the plasmonic properties of the TiN film by maximizing negative Re (ε) while keeping the losses as low as possible by minimizing Im (ε). As was done in Refs. [12,13], we can extract the frequency dependent optical properties of the resulting film using Ellipsometric measurements taken with Woollam WVASE32 vertical angle spectroscopic rotating-analyzer. Measurements were taken at three different incidence angles: 55°, 65°, and 75°. The Drude-Lorentz [14,15] model was then used to fit the data. Similar to the model presented in [5], our model consists of a Drude oscillator (damping (Γ_D) = 0.3 and plasma frequency (ω_p) = 6.5) representing the free d-band conduction electrons [16], two Lorentz oscillators representing the inter-band losses (energy (ω_0) = 4.35 and 2.52, damping (γ) = 1.48 and 1.14, oscillator strength (ω_l^2) = 37.6 and 2.6 respectively), and a background offset (ε_∞) of 4.16 representing the high energy inter-band transitions. More details about the sputtering process, stoichiometry, chemical composition, and carrier concentrations of our TiN films can be found in our previous publications [1,7,12]. Figure 1(a) compares the real and imaginary part of the measured dielectric function of our TiN to that of Au using values from Ref. [17]. Our TiN thin film exhibits both strong metallic behavior with high negative Re (ε) values, close to that of Au, as well as very low losses, manifested in the low values of Im (ε). In order to understand SPP coupling in our structures, we study the dispersion relation of the plasmon modes at the interface between TiN and air as well as TiN and MgO at different frequency regimes. For thin metallic films (40 nm TiN in our case), cross talk between the plasmonic modes across both interfaces (Air/TiN and TiN/MgO) is possible. At 650 nm, the evanescent decay length (confinement length normal to the surface) within the TiN can be calculated as $(2|k_1|)^{-1}$ where k_1 is the attenuation constant in TiN and is given by Eq. (1) with i = 1. For the modes excited at the MgO and air interfaces, this decay length is 30 nm and 35 nm respectively. These values increase at longer wavelengths. Therefore, for such a multilayer system, the TM modes in the core of the TiN are a superposition of two plane waves with the same propagation constant (the wave vector k_x is continuous across the thickness of the TiN with the same value at both interfaces) but with different attenuation constants in + z and –z, representing the superposition of the upper SPPs modes (Air/TiN interface) and the lower SPPs modes (TiN/MgO interface). Enforcing continuous solutions that satisfy the wave equation leads to four non-linear equations that represent the dispersion relation for a multilayer system [Eq. (1) with i = 1, 2, and 3, and Eq. (2)] [18]:

$$k_i^2 = k_x^2 - k_0^2 \varepsilon_i \ (i = 1,\ 2,\ 3) \tag{1}$$

$$e^{-4k_1 a} = \frac{\frac{k_1}{\varepsilon_1} + \frac{k_2}{\varepsilon_2}}{\frac{k_1}{\varepsilon_1} - \frac{k_2}{\varepsilon_2}} \frac{\frac{k_1}{\varepsilon_1} + \frac{k_3}{\varepsilon_3}}{\frac{k_1}{\varepsilon_1} - \frac{k_3}{\varepsilon_3}} \tag{2}$$

k_x is the propagation constant of the SPPs at either interface of a thin film with thickness 2a. k_1, k_2, and k_3 are the attenuation constants in TiN, MgO, and air respectively. k_0 is the propagation constant of the incident plane wave freely propagating mode in air that is used to couple to the SPPs, and is equal to $\frac{\omega}{c_0}$ where ω and c_0 are the angular frequency and the free space velocity of the incident plane wave. Solving Eq. (1) (with i = 1, 2, and 3) and Eq. (2) results in multiple frequencies (modes) for each value of the wave vector, k_x. Figure 1(b) shows finite difference time domain (FDTD) simulations of the plasmonic dispersion relation for our TiN multilayer insulator-metal-insulator (IMI) system for the case of Air/TiN/MgO (excitation is initiated from the air side) and MgO/TiN/Air (excitation is initiated from MgO side). In addition, the dispersion

Optics EXPRESS

relation of the SPPs on a single interface between two infinite mediums is overlaid as dotted white and black lines for the case of Air/TiN and MgO/TiN respectively. To obtain these graphs, Air/TiN/MgO were placed within the Lumerical FDTD simulation domain terminated with Bloch boundary conditions (BCs). We place a cloud of dipoles with different phase and orientation within the simulation domain. We then sweep over different values of the wave vector k_x and for each value we find the frequencies at which strong electric field resonance is observed. It is worth mentioning here that the simulation time should be long enough to allow for complete attenuation of the modes that are not supported by the structure. The air light-line and the MgO light-line represent the dispersion relations of the free propagating plane wave in air and MgO, respectively. On the left of the air light-line lies the TiN bulk plasmon band. On the right of the light-line we see the dispersion relation of the SPPs in the case of the Air/TiN/MgO system centered on the Air/TiN single interface dispersion relation (dotted white line). At low frequencies, the SPP of the Air/TiN/MgO system is represented by a line that coincides with the air line, whereas at higher frequencies that line branches into a band of frequencies representing multiple modes (different possible frequencies for the same value of the wave vector) centered on the single interface SPP dispersion relation. This band is represented by the faded white area in Fig. 1(b) between the labels "high frequency odd modes" and "low frequency even modes." The solutions with frequencies higher than the single interface SPPs exhibit odd vector parity

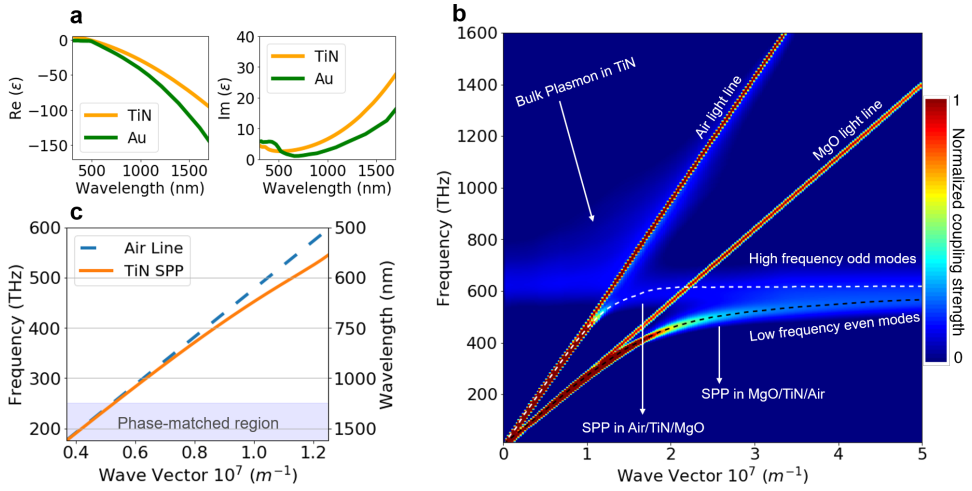

Fig. 1. (a) Real and Imaginary part of the dielectric function of Au and our sputtered TiN thin film on MgO substrate obtained by spectroscopic ellipsometry, showing the close resemblance between both Re (ε) and Im (ε) of our optimized TiN thin films and those of Au. (b) FDTD numerical simulations of the surface plasmon band diagram in IMI system with the dispersion relation of single interface overlaid as dotted white and black lines for the case of Air/TiN and MgO/TiN respectively. This plot was obtained using FDTD simulations by sweeping over the wave vector to find corresponding frequencies at which the coupled electric field is maximized. The change in color along the SPP trace reflects the strength of the resonance at each point. For small wave vectors (dark red color), each wave vector has strong coupling at a single corresponding frequency. As the value of the wave vector increases the corresponding resonance branches from being one frequency point to a band of different resonance frequencies (faded turquoise region in the plot representing different frequencies at which strong coupling is observed where the strength of the coupling is determined by the scale bar) (c) Zoom in from Fig. 1(b) showing the dispersion relation at the frequency band of interest in the Air/TiN/MgO interface.

Optics EXPRESS

(H_y *is even*, E_x *is odd*, E_z *is even*) [18]. On the other hand, the solutions with frequencies lower than the single interface SPPs exhibit even vector parity (H_y *is odd*, E_x *is even*, E_z *is odd*). The asymmetry of the dielectric interfaces (lower MgO medium and upper Air medium) allows for a hybridized surface plasmon polariton mode (coupled modes of the individual constitutive modes at each interface) in the TiN thin film which has been shown to be promising for long range propagation [19–22]. Figure 1(c) is a magnified representation of the lower left-corner of Fig. 1(b) for the Air/TiN/MgO interface, showing the discrepancy between the values of the wave vector for frequencies higher than 250 THz. Because of the phase- (momentum-) mismatch between the free air modes and the confined SPPs modes [Fig. 1(c)], grating structures are used to couple the incoming optical excitation to the SPPs at the surfaces of the TiN thin films. Lumerical FDTD simulations were used to optimize the dimensions (thickness, width of the grating lines, and the pitch) of a dielectric grating made of a ZEP-based electron beam resist (frequency dependent refractive index given by the manufacturer [23]).

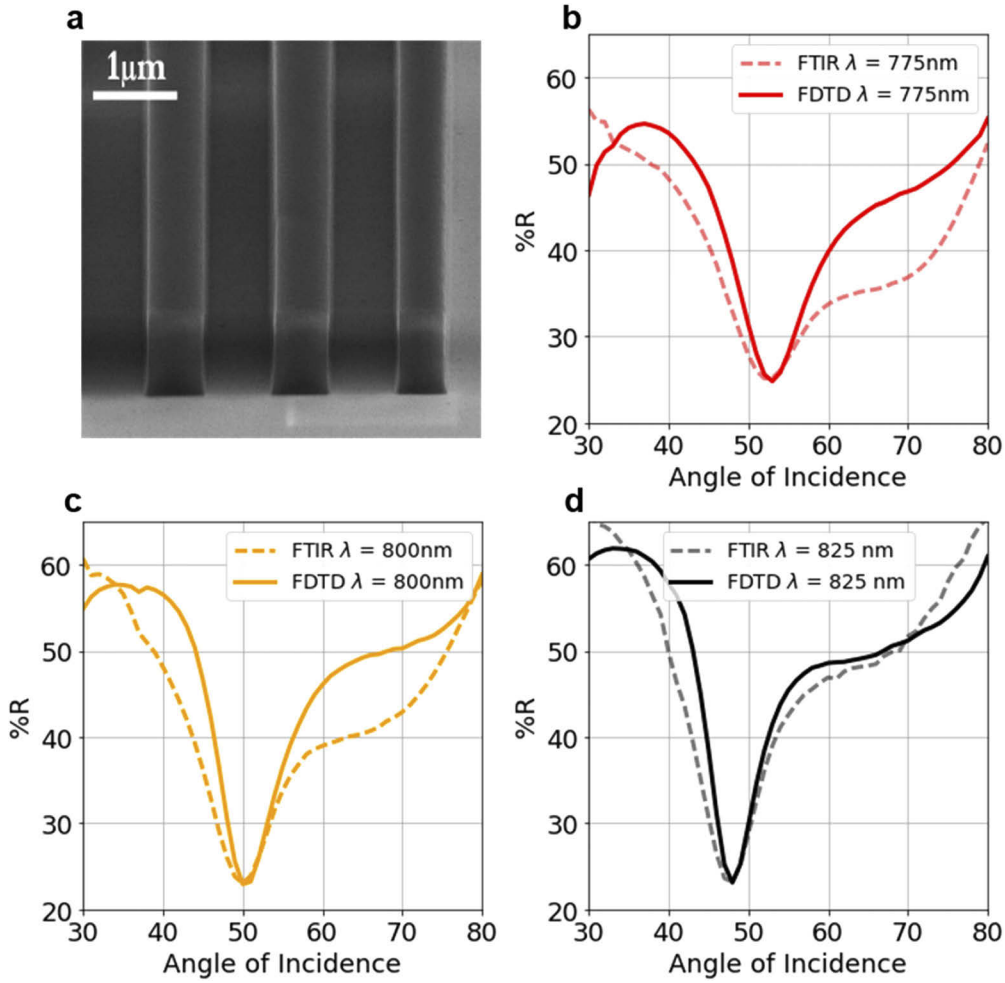

Fig. 2. (a) Grating used for momentum matching. (b,c,d) far-field reflectivity at 775 nm, 800 nm, and 825 nm respectively at different angles of incidence showing strong coupling to SPPs in TiN in the visible regime. Measurements are labeled as FTIR and simulations are labeled as FDTD.

Optics EXPRESS

The simulations predicted the optimal grating thickness to be 300 nm, line width to be 750 nm, and the pitch to be 1500 nm. Figure 2(a) shows the fabricated grating using electron beam lithography on the top of a 40 nm TiN thin film. J.A.Woollam ellipsometer was used to illuminate the grating with p-polarized light (magnetic field parallel to the grating) at three wavelengths, 775 nm, 800 nm, and 825 nm. At each wavelength, the angular reflectance was recorded at different angles of incidence ranging from 30° to 80°. The reported significant dips in the measured far field reflectance [Figs. 2(b), 2(c), and 2(d)] are indicative of the coupling to SPP resonances that can be tuned by changing the angle of incidence or the grating dimensions. The comparison between experimental measurements and numerical simulations presented in Fig. 2 shows a good agreement, especially for the spectral location of the resonance angle. The far-field reflection data shown in Fig. 2 provide good evidence of SPP resonances in the Air/TiN/MgO structure. Nevertheless, we seek further, more detailed confirmation of the SPP resonances by using spatially-resolved near field imaging of the SPPs.

3. Near-field spectroscopy for visible and infrared (spoof) surface plasmon polaritons

We employ a collection mode Scanning Near-Field Optical Microscope (SNOM, Nanonics Imaging Ltd), which probes the near fields of the SPPs with a metallized tapered fiber optic tip having an effective diameter of ~ 50 nm. Since the collection is made from the air-side of the Air-TiN-MgO structure, illumination is carried out from the MgO side using a super continuum laser (NKT Photonics) with a filter (NKT Select) to provide excitation at 775 nm, 800 nm, and 825 nm. The measurement set-up is illustrated in Fig. 3(a). In order to couple the incoming optical excitation to the SPPs, we form a 200 nm wide slit in the TiN thin film. Diffraction theory predicts that the transmission of a single value wave vector through a finite slit produces an infinite number of wave vectors with different magnitudes and different directions. The match between the wave vectors scattered from the slit and the SPP modes will create the propagating SPP resonances. In this measurement setup, although the excitation is from the MgO side, the SPPs are excited and detected at the TiN/Air interface where the momentum matching condition is satisfied via the slit that acts as a source of infinite wave vectors. Therefore, the modes excited via the grating (far field measurements in Fig. 2) and the slit (near field measurements in Fig. 3) are the same.

Figure 3(b) is an FDTD simulation of the SPP resonances in the regions surrounding the slit. The SNOM experiments presented in Figs. 3(c)–3(e) show the near fields imaging corresponding to excitation wavelengths of 775 nm, 800 nm and 825 nm, respectively. Clearly visible is the bright intensity from the region of the slit, as well as the distinctive fringes of the SPPs modes on the surface of the TiN thin film. The fringes arise from the interference between the SPPs and the transmitted beam, and the fringe spacings give the SPP wavelengths, 742 nm, 765 nm, and 791 nm, corresponding to excitation wavelengths of 775 nm, 800 nm, and 825 nm, respectively. These values agree very well with the FDTD simulations and theoretical calculations ($\lambda_{SPP} = \frac{2\pi}{k_x}$, where the value of k_x is obtained from Fig. 1(b) from the MgO/TiN/Air interface). More importantly, the excellent optical properties of the TiN are manifested in the long propagation lengths of the SPPs. We define the propagation length as the distance between the launch point to the point at which the mode power decays by a factor of 1/ e. The field of view of the SNOM limits the scan range to what is shown in Figs. 3(c)–3(e). The insets of Figs. 3(c)–3(e) show E-Field intensity decay by a factor of around Exp(-0.5) over a 5 μm distance. Therefore, for each of the excitation wavelengths, we detected propagation lengths of at least 10 μm. This value agrees with the theoretical expectation of the propagation length which can be calculated as $(2\beta_x)^{-1}$, where $\beta_x = \frac{2\pi}{\lambda_{air}}\sqrt{\frac{\varepsilon_{metal} \times \varepsilon_{air}}{\varepsilon_{metal} + \varepsilon_{air}}}$ [18]. The main limitation for the propagation length here is not just the metallic losses but also the radiation losses due to the surface roughness of the

Optics EXPRESS

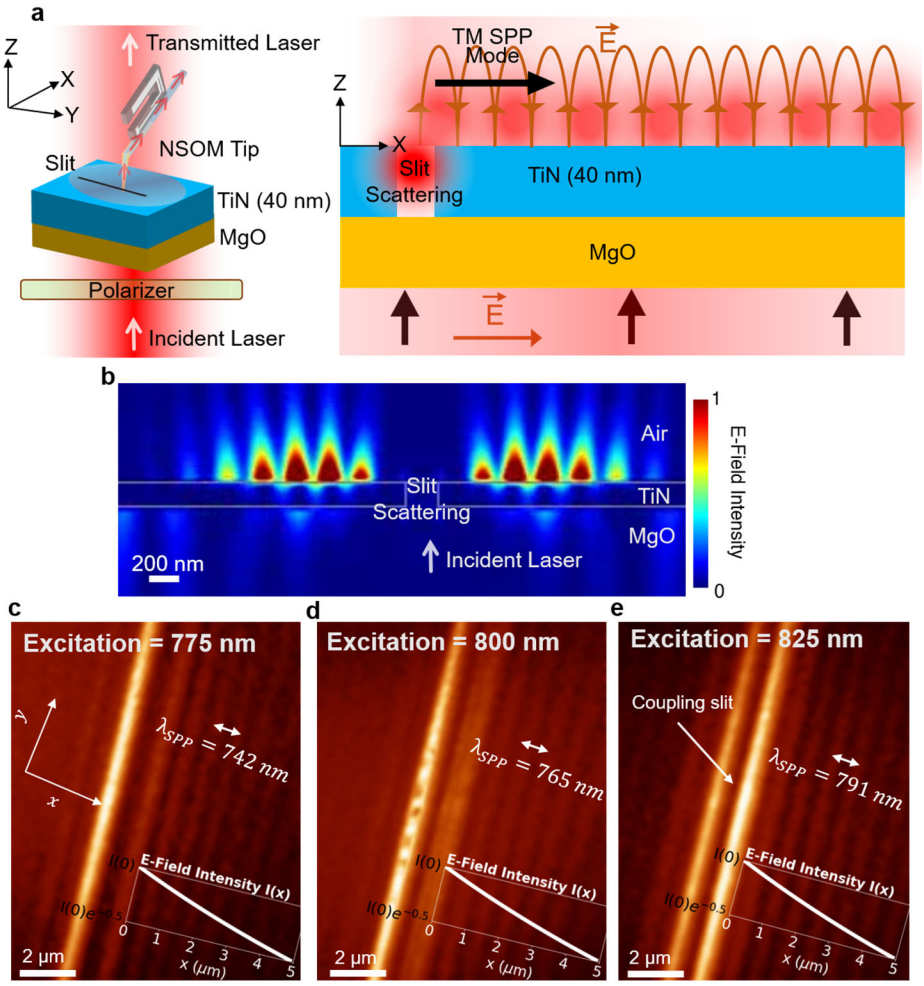

Fig. 3. (a) SNOM measurement procedure (b) FDTD simulations for SPPs on TiN using slit coupling at 825 nm excitation. (c,d,e) SNOM results showing actual images of the SPPs with long propagation length of at least 10 μm for three excitation wavelengths: 775 nm, 800 nm, and 825 nm. Fast Fourier Transform of the data presented shows a dominant peak that corresponds to the periodicity of the fringes. The insets of figure c, d, and e labeled E-Field Intensity I(x) show the exponential power decay as a function of propagation distance x.

metallic thin film. This radiation loss can be overcome, thus increasing the propagation length to even centimeter range [24], by sandwiching the metallic thin film between two dielectrics with carefully designed dimensions creating a plasmonic waveguide as has been done previously [19–21,25,26]. Figure 3 gives evidence of a propagation length of 10 μm at 775 nm which is relatively longer than previously-reported propagation lengths in bare metallic TiN thin films [3,5]

Figure 1(b) and the images shown in Figs. 2 and 3 demonstrate that TiN thin films can support robust SPPs with $\lambda_{SPP} \sim 750$–800 nm. However, at the longer wavelengths, such as in the mid-IR, pertaining to the "phase-matched" region shown in Fig. 1(c) (< 250 THz or ~ 1.2 μm wavelength), SPPs are not supported. The metallic TiN behaves as a perfect electric conductor, with an electric field value dropping to zero at the interface, and the surface modes couple to radiative modes in

Optics EXPRESS

the phase-matched region, also resulting in the loss of SPP confinement. However, Pendry et al. [27] realized that patterning the surface of the plasmonic material with etched holes or grooves whose lateral dimensions are smaller than the wavelengths of interest creates an *effective medium* that satisfies the conditions needed for confined surface wave excitations [28]. The patterned surface mimics or "spoofs" the behavior of metals in the visible regime, and these excitations are termed *Spoof Surface Plasmon Polaritons (SSPPs).* Previous experimental detection of SSPPs [29–31] have demonstrated that a significant depth of the trenches is necessary so that the grooves act as a cavity for the surface modes thus reducing their group velocity and strongly increasing their confinement at the interface. We explore the excitation of these SSPPs at 6 μm using a 1D array of air-filled grooves etched into our TiN of width a, period d, and etched depth h. As explained in [32,33], the dispersion relation of SSPP TM modes in such effective homogenous anisotropic media is given by Eq. (3). Additionally, the complex wave vector (k_g) of the evanescent fields inside the waveguide is given by Eq. (4).

$$k_x{}^2 = k_0{}^2 + \left(\frac{ak_g tan\,(hk_g)}{d}\right)^2 \tag{3}$$

$$k_g{}^2 = k_0{}^2\left(1 + \frac{i+1}{ak_0 Re\sqrt{-\epsilon_{TiN}}}\right) \tag{4}$$

k_0 is the wave vector of the incident free modes in air, k_g is the complex wave vectors of the evanescent modes propagating inside the guide, and k_x is the wave vector of the SSPPs confined modes propagating at the surface of the TiN grooves. Equations (3) and (4) provide greater accuracy than other analytical analyses that treat the metal as a perfect electric conductor [27,34], because they allow to explicitly incorporate the optical properties of TiN (ϵ_{TiN}) which

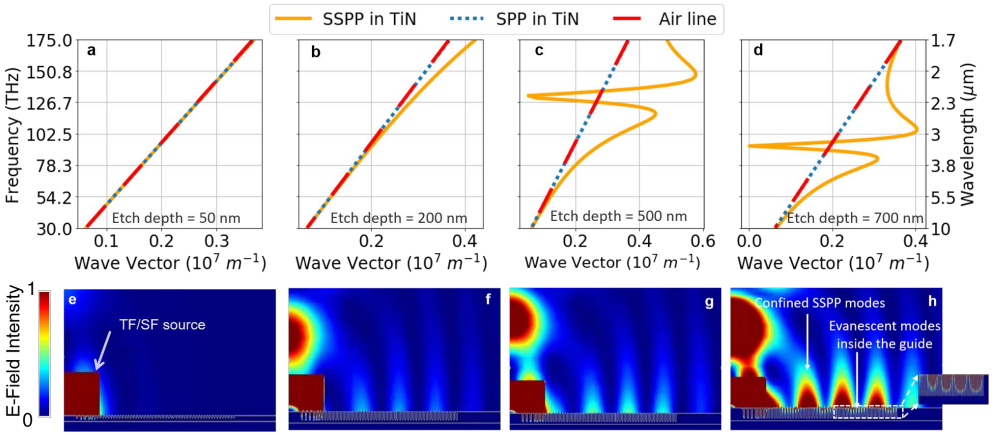

Fig. 4. (a, b, c, d) dispersion relation of SSPP at 50 nm, 200 nm, 500 nm, and 700 nm etch depth respectively. (e,f,g,h) Corresponding FDTD simulations showing the coupling from a 6 μm Total Field / Scattered Field excitation source (TF/SF) to SSPP on the surface of 50 nm, 200 nm, 500 nm, and 700 nm etch depth respectively. The red blob propagating upwards in plots f, g, and h represents reflections from the normally incident source. Figure h clearly shows the confined high intensity SSPP modes and the exponential evanescent behavior experienced inside the waveguides. The inset of Figure h shows a zoom in on the evanescent modes inside the trenches with saturated scale bar to highlight their decay behavior inside the guide. Visualization 1, Visualization 2, and Visualization 3 show the temporal evolution of the spoof plasmons for different etch depths in addition to the coupling and decoupling of radiative and confined states as the modes transition between flat and etched surfaces.

Optics EXPRESS

we measured experimentally using spectroscopic ellipsometry. We investigate the effect of etch depth on the dispersion relation of SSPP [Eqs. (3) and (4)] with a grating period of 200 nm and line width of 100 nm. Figures 4(a), 4(b), 4(c), and 4(d) plot the dispersion relation of SSPPs in the near to mid infrared for etch depths of 50 nm, 200 nm, 500 nm, and 700 nm. Figure 4(a) shows that for an etch depth of 50 nm, the phase of air modes, SPPs and SSPPs are the same, indicating the impossibility of exciting any confined modes because of immediate coupling of surface waves to radiative modes. This is confirmed by the FDTD simulation presented in Fig. 4(e) showing no surface modes at 6 μm illumination. As we increase the etch depth [Figs. 4(b), 4(c), and 4(d)] we observe that the value of the momentum of the SSPPs deviates from that of SPPs and air modes suggesting the possibility of exciting confined surface modes at mid- IR. These calculations show that to achieve acceptable coupling at 6 μm wavelength, a minimum etch depth of 700 nm is needed. The field profiles from the FDTD simulations for 200 nm, 500 nm, and 700 nm etch depths [Figs. 4(f), 4(g), and 4(h)] confirm these results by showing the negligible coupling for etch depths below 700 nm. Accordingly, we fabricated 700 nm deep grooves with a = 100 nm and d = 200 nm using Electron Beam Lithography and Inductively coupled plasma Reactive Ion

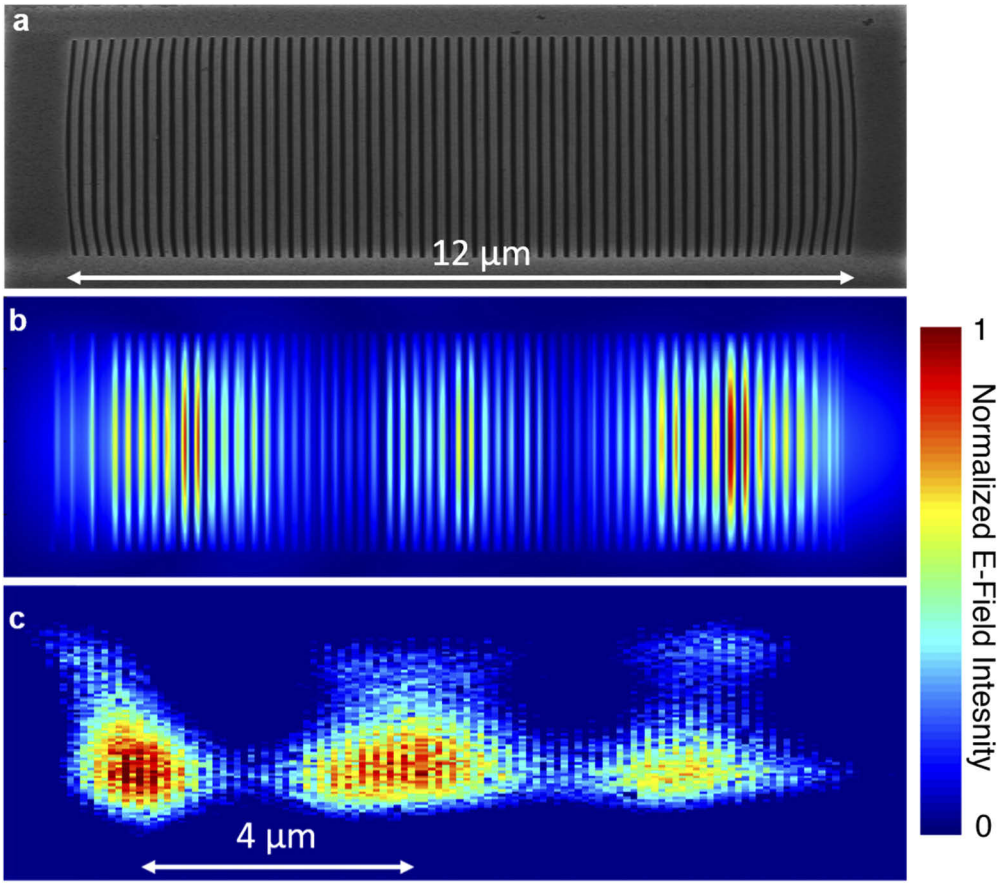

Fig. 5. (a) 700 nm deep grooves in TiN fabricated using Ebeam lithography and ICP-RIE etching. (b) Top view for the FDTD simulations of the expected spoof plasmon modes at 6 um illumination. (c) Near field imaging of the strongly excited plasmons for a grating line width of 100 nm and a period of 200 nm. The nonuniformity of the measured field pattern in figure c is due to the degradation of the tip as it scans the trenches with significantly high aspect ratio.

Optics EXPRESS

Etching (ICP-RIE) on a 1 μm thick TiN thin film. To experimentally validate the simulations, we obtained spatially-resolved near field images of the SSPPs in the patterned TiN film. We obtained such images by carrying out apertureless scattering-type Scanning Near-field Optical Microscopy (s-SNOM) of 12 μm long etched trenches as shown in Fig. 5(a). The results of these measurements presented in Fig. 5(c) show strong SSPPs coupling with fringe spacing of 4 μm. Figures 5(b) and 5(c) show a close match between our FDTD predictions and the near field measurements, confirming the excitation of confined surface plasmon modes in TiN at 6 μm illumination. The fringes observed in the simulations of the electric field profile of the spoof plasmons [Fig. 5(b)] are due to the excitation of standing SSPP waves. As the SSPPs make the transition from the trench surface to the unpatterned surface, they experience reflections due to the change in effective index between the two regions, resulting in a standing wave behavior.

As done in our previous study of localized surface plasmon in TiN nano-antennas on silicon [1], our s-SNOM analysis utilized a silicon tip coupled to an Atomic Force Microscopy (AFM) system, allowing for high spatial resolution 3D movement of the tip around the structure. The grating is illuminated by a 6 μm wavelength light source (a narrow-band quantum cascade laser, QCL) through a Michelson interferometer at an incidence angle of 60°. The silicon tip, in tapping mode on the sample, becomes polarized by the laser source and itself acts as a local antenna that scatters the near field from the surface of the grating, modulating the light with the tapping frequency. A moving mirror, oscillating at the same frequency as the tip is used to implement pseudo-heterodyne demodulation of the phase and amplitude of the scattered field. Images of amplitude, such as that shown in Fig. 5(c), are formed by raster scans of the tip over the grating's surface in the (x, y) plane. This setup allows for the detection of the magnitude and phase of the out-of-plane electric field component (E_z) only. It is worth mentioning that because of the high aspect ratio of the grating, the tip gets damaged during the scanning and often breaks down before the end of the scan. Several measurements had to be taken to be able to scan a 12 μm long grating, during which the tip quality was degraded, resulting in the non-uniform E-field pattern in Fig. 5(c).

4. Conclusion

We have demonstrated the plasmonic capabilities of TiN thin films deposited under conditions that produced high metallic quality *and* low loss. Such films produced strong SPP resonances, which we were able to directly image in the near field for both visible and infrared wavelengths. Near-field imaging indicates propagation lengths longer than 10 μm, We note that although previous reports [3,5,35] have presented mathematical calculations for SPP propagation lengths in TiN thin films, no experimental imaging of the plasmons nor measurements of their propagation lengths have been hitherto reported. Additionally, we explored the excitation of Spoof SPPs on the surface of our TiN thin films in the mid-IR region, and provided near-field images using scattering s-SNOM.

Funding

National Science Foundation (1839164-PHY: RAISE-TAQS, ECCS-1541959, ECCS-1748106: EAGER).

Acknowledgments

The authors gratefully acknowledge Andy Greenspon, Michele Tamagnone and Stephan Kraemer discussions on fabrication and measurements.

Optics EXPRESS

Disclosures

The authors declare no conflicts of interest.

References

1. M. N. Gadalla, A. S. Greenspon, M. Tamagnone, F. Capasso, and E. L. Hu, "Excitation of Strong Localized Surface Plasmon Resonances in Highly Metallic Titanium Nitride Nano-Antennas for Stable Performance at Elevated Temperatures," ACS Appl. Nano Mater. **2**(6), 3444–3452 (2019)..
2. U. Guler, A. Boltasseva, and V. M. Shalaev, "Refractory plasmonics," Science **344**(6181), 263–264 (2014).
3. G. V. Naik, J. L. Schroeder, X. Ni, A. V. Kildishev, T. D. Sands, and A. Boltasseva, "Titanium nitride as a plasmonic material for visible and near-infrared wavelengths," Opt. Mater. Express **2**(4), 478–489 (2012).
4. U. Guler, D. Zemlyanov, J. Kim, Z. Wang, R. Chandrasekar, X. Meng, E. Stach, A. V. Kildishev, V. M. Shalaev, and A. Boltasseva, "Plasmonic Titanium Nitride Nanostructures via Nitridation of Nanopatterned Titanium Dioxide," Adv. Opt. Mater. **5**(7), 1600717 (2017).
5. H. Reddy, U. Guler, Z. Kudyshev, A. V. Kildishev, V. M. Shalaev, and A. Boltasseva, "Temperature-Dependent Optical Properties of Plasmonic Titanium Nitride Thin Films," ACS Photonics **4**(6), 1413–1420 (2017)..
6. G. V. Naik, B. Saha, J. Liu, S. M. Saber, E. A. Stach, J. M. Irudayaraj, T. D. Sands, V. M. Shalaev, and A. Boltasseva, "Epitaxial superlattices with titanium nitride as a plasmonic component for optical hyperbolic metamaterials," Proc. Natl. Acad. Sci. **111**(21), 7546–7551 (2014)..
7. C. M. Zgrabik and E. L. Hu, "Optimization of sputtered titanium nitride as a tunable metal for plasmonic applications," Opt. Mater. Express **5**(12), 2786–2797 (2015)..
8. W.-P. Guo, R. Mishra, C.-W. Cheng, B.-H. Wu, L.-J. Chen, M.-T. Lin, and S. Gwo, "Titanium Nitride Epitaxial Films as a Plasmonic Material Platform: Alternative to Gold," ACS Photonics **6**(8), 1848–1854 (2019)..
9. R. P. Sugavaneshwar, S. Ishii, T. D. Dao, A. Ohi, T. Nabatame, and T. Nagao, "Fabrication of highly metallic TiN films by pulsed laser deposition method for plasmonic applications," ACS Photonics **5**(3), 814–819 (2018).
10. N. Kinsey, M. Ferrera, G. V. Naik, V. Babicheva, V. M. Shalaev, and A. Boltasseva, "Experimental demonstration of titanium nitride plasmonic interconnects," Opt. Express **22**(10), 12238–12247 (2014).
11. C. Vernoux, Y. Chen, L. Markey, C. Spârchez, J. Arocas, T. Felder, M. Neitz, L. Brusberg, J.-C. Weeber, and S. I. Bozhevolnyi, "Flexible long-range surface plasmon polariton single-mode waveguide for optical interconnects," Opt. Mater. Express **8**(2), 469–484 (2018).
12. C. M. Zgrabik, *Wide tunability of magnetron sputtered titanium nitride and titanium oxynitride for plasmonic applications* (2016).
13. M. Gadalla, A. Greenspon, M. Tamagnone, F. Capasso, and E. Hu, "Metallic refractory titanium nitride: An alternative stable metal with tunable optical properties for high temperature plasmonic applications," in *APS Meeting Abstracts* (2019).
14. N. White, A. Campbell, J. Grant, R. Pachter, K. Eyink, R. Jakubiak, G. Martinez, and C. Ramana, "Surface/interface analysis and optical properties of RF sputter-deposited nanocrystalline titanium nitride thin films," Appl. Surf. Sci. **292**, 74–85 (2014).
15. J. Rivory, J. Behaghel, S. Berthier, and J. Lafait, "Structure and properties of TiN coatings," Thin Solid Films **78**(2), 161–165 (1981).
16. P. Patsalas and S. Logothetidis, "Optical, electronic, and transport properties of nanocrystalline titanium nitride thin films," J. Appl. Phys. **90**(9), 4725–4734 (2001)..
17. W. M. Haynes, *Crc handbook of chemistry and physics* (CRC press, 2014).
18. S. A. Maier, *Plasmonics: Fundamentals and applications* (Springer Science & Business Media, 2007).
19. J. Chen, Z. Li, S. Yue, and Q. Gong, "Hybrid long-range surface plasmon-polariton modes with tight field confinement guided by asymmetrical waveguides," Opt. Express **17**(26), 23603–23609 (2009).
20. M.-S. Tomaš and Z. Lenac, "Long-range surface polaritons in a supported thin metallic slab," Solid State Commun. **50**(10), 915–918 (1984).
21. M.-S. Tomaš and Z. Lenac, "Coupled surface polariton with guided wave polariton modes in asymmetric metal clad dielectric waveguides," Opt. Commun. **55**(4), 267–270 (1985).
22. Z. Lenac, "Attenuation of long-range surface polaritons in a thin metallic slab with a dielectric coating," Surf. Sci. **154**(2-3), 639–657 (1985).
23. http://www.nanophys.kth.se/nanophys/facilities/nfl/resists/zep520a-7-2.pdf.
24. P. Berini, "Long-range surface plasmon polaritons," Adv. Opt. Photonics **1**(3), 484–588 (2009).
25. W. Ma and A. S. Helmy, "Asymmetric long-range hybrid-plasmonic modes in asymmetric nanometer-scale structures," J. Opt. Soc. Am. B **31**(7), 1723–1729 (2014)..
26. S. Saha, A. Dutta, N. Kinsey, A. V. Kildishev, V. M. Shalaev, and A. Boltasseva, "On-Chip Hybrid Photonic-Plasmonic Waveguides with Ultrathin Titanium Nitride Films," ACS Photonics **5**(11), 4423–4431 (2018)..
27. J. Pendry, L. Martin-Moreno, and F. Garcia-Vidal, "Mimicking Surface Plasmons with Structured Surfaces," Science **305**(5685), 847–848 (2004).
28. M. Born and E. Wolf, *Principles of optics: Electromagnetic theory of propagation, interference and diffraction of light* (Elsevier, 2013).

Optics EXPRESS

29. N. Yu, Q. J. Wang, M. A. Kats, J. A. Fan, S. P. Khanna, L. Li, A. G. Davies, E. H. Linfield, and F. Capasso, "Designer spoof surface plasmon structures collimate terahertz laser beams," Nat. Mater. **9**(9), 730–735 (2010).
30. J. Y. Yin, J. Ren, H. C. Zhang, B. C. Pan, and T. J. Cui, "Broadband Frequency-Selective Spoof Surface Plasmon Polaritons on Ultrathin Metallic Structure," Sci. Rep. **5**(1), 8165 (2015)..
31. Z. Liao, Y. Luo, A. I. Fernández-Domínguez, X. Shen, S. A. Maier, and T. J. Cui, "High-order localized spoof surface plasmon resonances and experimental verifications," Sci. Rep. **5**(1), 9590 (2015)..
32. A. Rusina, M. Durach, and M. I. Stockman, "Theory of spoof plasmons in real metals," Appl. Phys. A **100**(2), 375–378 (2010).
33. A. Rusina, M. Durach, K. A. Nelson, and M. I. Stockman, "Nanoconcentration of terahertz radiation in plasmonic waveguides," Opt. Express **16**(23), 18576–18589 (2008).
34. F. Garcia-Vidal, L. Martin-Moreno, and J. Pendry, "Surfaces with holes in them: new plasmonic metamaterials," J. Opt. A: Pure Appl. Opt. **7**(2), S97–S101 (2005).
35. M. Cortie, J. Giddings, and A. Dowd, "Optical properties and plasmon resonances of titanium nitride nanostructures," Nanotechnology **21**(11), 115201 (2010).